Title
4D Flow with Compressed Sensing for the Evaluation of Intracranial Aneurysmal Flow Patterns

Author
Hinostroza, Virginia

Publication Date
2019

Peer reviewed|Thesis/dissertation

4D Flow with Compressed Sensing for the Evaluation of Intracranial Aneurysmal Flow Patterns

by
Virginia Hinostroza

THESIS
Submitted in partial satisfaction of the requirements for degree of
MASTER OF SCIENCE

in

Biomedical Imaging

in the

GRADUATE DIVISION
of the
UNIVERSITY OF CALIFORNIA, SAN FRANCISCO

Approved:

DocuSigned by:
F1B602CAB7874F1...
David Saloner
Chair

DocuSigned by:
Amans, Matthew
Amans, Matthew

DocuSigned by:
Jing Liu
Jing Liu

DocuSigned by:
Haraldsson, Henrik
Haraldsson, Henrik

Committee Members

ACKNOWLEDGEMENTS & DEDICATION

I would like to first thank my thesis committee chair, David Saloner, PhD, for his guidance in exploring the technical aspects of one of the most remarkable imaging techniques I have come across. Many thanks to my other committee members: Henrik Haraldsson, PhD for his extensive mentorship and patience at each and every step, as well as to Jing Liu, PhD, and Matthew Amans, MD, for sharing their expertise as I engaged with all the data produced by this project. Other lab members, including Evan Kao, PhD, Chengcheng Zhu, PhD, Dimitrios Mitsouras, PhD, Xinke Liu, MD, and Fei Xiong, MS, provided much help and feedback throughout this endeavor.

The MSBI faculty set the groundwork for this study; doing so in such a short period of time is no easy feat, but I am certain the skills and tools they equipped us with will be invaluable in the future. My classmates have inspired and challenged me daily; I would not have made it here without them and look forward to seeing all the amazing things they will achieve in the future.

I am especially indebted to Dominik Fleischmann, MD, who first introduced me to the field of radiology and cardiovascular imaging, and Frandics Chan, MD, who has been my most ardent supporter throughout this program. My achievements could not have been possible without the mentorship of Kathrin Baeumler, PhD, and Benjamin Zahneisen, PhD, who managed to turn the hardest problem sets into some of the most enjoyable learning experiences.

Last, but certainly not least, I extend my heartfelt gratitude to my family and friends. This project is dedicated to my immediate family – Julio, Elza, George and Julie – who have been unwavering in their support throughout the years. I am extremely grateful to Joseph Woodard, for his patience and constant encouragement as I ventured on my educational and professional journeys. My friends – too many to list individually – have also been incredibly supportive and they will be glad to know I can *finally* understand (most of) what they are talking about.

4D Flow with Compressed Sensing for the Evaluation of Intracranial Flow Patterns

Virginia Hinostroza

ABSTRACT

Background: 4D flow (4DF) magnetic resonance imaging (MRI) offers a promising way to evaluate blood flow patterns in intracranial aneurysms, although long scan times present a major limitation to broad clinical implementation. Compressed sensing (CS), an accelerated imaging technique using strategically undersampled data for data reconstruction, offers a possible solution to reduce scan times. The aim of this study was to understand the effects and limitations of varying compressed sensing acceleration factors, R, at different resolutions in *in vitro* 4D flow acquisitions.

Methods: This study employed a phantom depicting a saccular aneurysm. Experiment 1 evaluated the reliability of 4D flow with varying levels of compressed sensing acceleration factors (R=7.6, 12.8, and 16.6). Experiment 2 assessed the effects of varying resolutions (0.5, 1.0, 1.5, and 2.0 mm) with a compressed sensing R=12.8. Qualitative analysis included a visual assessment of velocity vectors and streamlines. Quantitative analysis compared the velocity components, peak velocity, flow rate, and wall shear stress in each experiment. All studies were post-processed using a clinically-geared software as well as with an In-House engineering pipeline, with the purpose of understanding the advantages and disadvantages of each approach and validating any results.

Results: The addition of compressed sensing reduced scan times to approximately 4-7 minutes. The In-House processing pipeline is superior to the clinical software in visualizing of velocity; visual analysis showed velocity overestimations in the R=16.8 streamlines, indicating the limits of compressed sensing to be $7.6 < R < 12.8$. As expected, comparison of velocity components reflects a decrease in linear regression slopes and correlations as acceleration factors increased ($m > 0.90$ for all acceleration factors except R=16.6, and all $r > 0.9$). Experiment 2 highlights partial

voluming effect at R=12.8: as resolutions decrease, velocities along the wall are less reliable than velocities furthest from the wall, which retain high slope and correlation values (both above 0.9 at 1.0 mm and 1.5 mm resolutions). High variability peak velocity, flow rate, and wall shear stress in both pipelines point to the need for a reliable way to post-process 4D flow.

Conclusion: This study showed reliable velocity data can be obtained from 4D flow studies acquired with compressed sensing lower to moderate acceleration factors at higher resolutions. With clinically-acceptable scan times, the focus now shifts towards establishing a robust and validated workflow for 4D flow studies before clinical implementation can truly be feasible.

TABLE OF CONTENTS

1. INTRODUCTION 1

1.1 Intracranial Aneurysms and Risk Rupture 1

1.2 Hemodynamics of Intracranial Aneurysms 1

1.3 4D Flow and Its Limitations 2

1.4 Compressed Sensing 3

1.5 Objective 4

2. MATERIALS AND METHODS 4

2.1 *In vivo* Three-Dimensional Phantom 4

2.2 Study Design for Experiments 1 and 2 5

2.3 4D Flow MR Acquisitions 5

2.4 Flow Parameters Evaluated 6

2.5 Post-Processing 6

2.6 Visualization of Velocity Vectors and Streamlines 7

2.7 Velocity Vector Components 7

2.8 Peak Velocity, Flow Rate, Wall Shear Stress 8

2.9 Data Analysis 9

3. RESULTS 10

3.1 Visualization of Velocity Vectors and Streamlines 10

3.1.1 Experiment 1: Visualization of Velocity Vectors and Streamlines 11

3.1.2 Experiment 2: Visualization of Velocity Vectors and Streamlines 12

3.2 Comparison of Velocity Components....13
3.2.1 Experiment 1: Velocity Components at Different Compressed Sensing Acceleration Factors....13
3.2.2 Experiment 2: Velocity Components of Different Resolutions at Compressed Sensing R=12.8....15
3.3 Peak Velocities, Flow Rates, and Wall Shear Stress....18
3.3.1 Experiment 1: Peak Velocities, Flow Rates, and Wall Shear Stress at Different Compressed Sensing Acceleration Factors....18
3.3.2 Experiment 2: Peak Velocities, Flow Rates, and Wall Shear Stress at Different Resolutions with Compressed Sensing R=12.8....19
4. DISCUSSION, FUTURE DIRECTIONS & CONCLUSION....21
4.1 Conclusion....25
5. REFERENCES....26

LIST OF FIGURES

Figure 2.1 Study design of Experiment 1 and Experiment 2 5

Figure 2.2 Strategy for comparison of velocity components 8

Figure 2.3 Planes of interest in CVI42 and In-House pipeline for the evaluation of peak velocity, flow rate, and wall shear stress 9

Figure 3.1 Experiment 1: Velocity vectors and streamlines at systole 11

Figure 3.2 Experiment 2: Velocity vectors and streamlines at systole 13

Figure 3.3 Experiment 1: Comparison of magnitude velocity components 14

Figure 3.4 Experiment 2: Comparison of magnitude velocity components 17

Figure 3.5 Experiment 1: Peak velocities, flow rates, and wall shear stress 19

Figure 3.6 Experiment 2: Peak velocities, flow rates, and wall shear stress 20

LIST OF TABLES

Table 2.1 Parameters of 4DF MR Acquisitions for Experiments 1 and 2 6

1. INTRODUCTION

1.1 Intracranial Aneurysms and Risk Rupture

Intracranial aneurysms are abnormal dilations along a localized section of a vessel, caused by a weakening in the wall structure.[1] Approximately 90% of intracranial aneurysms present as saccular,[2] which tend to form at junctions throughout the cerebral vascular system,[3] commonly around the cerebral base and along the circle of Willis.[4] The other 10% of intracranial aneurysms appear as fusiform or dissecting.[4] It is believed approximately 3% of the population have intracranial aneurysms,[5] although there are an increasing number of unruptured intracranial aneurysms are being detected, reflecting improvements in non-invasive imaging modalities such as magnetic resonance imaging (MRI) and computed tomography (CT) over the past decades.[6]

As with other vascular diseases, the main concern in the management of intracranial aneurysms is evaluating the risk of rupture. Although only 0.25% of aneurysms will eventually rupture,[5] they have been associated with serious outcomes, including subarachnoid hemorrhages with high rates of fatality (30-40%) and functional impairment, even in patients that survive.[7] Thus, clinicians must weigh the unlikely risk of rupture that comes with conservative clinical management against the associated risks of prophylactic endovascular and surgical interventions[8] and their associated costs.[9] Although scoring systems and guidelines consider a patient's demographics, medical history[10] and modifiable risk factors[5] when determining rupture risk, from an imaging standpoint, aneurysmal size has proven to be a consistent predictor of rupture.[6]

1.2 Hemodynamics of Intracranial Aneurysms

Although larger aneurysms are at greater risk for rupture, small aneurysms often do rupture as well,[11] underscoring the limitation of size as a prediction variable and the need to look for other measurable predictors. Recently there has been increased interest in gaining a deeper

understanding of hemodynamics and the role it plays in the etiology and progression of intracranial aneurysm, as well as its potential prognostic value to predict ruptures. Wall shear stress, the frictional and tangential force exerted by flowing blood on a vessel wall,[12] is of particular interest since there is evidence it plays a key role in the behavior and integrity of endothelial cells. Physiological levels of wall shear stress seem to support correct alignment and regulation of the inflammatory factors, with abnormal wall shear stress levels promoting aneurysm formation and expansion.[13] Sustained levels of high wall shear stress have been known to contribute to vascular disease pathogenesis,[13] causing endothelial injury that initiates vascular remodeling, a process that leaves the vessel wall susceptible to expansion.[14] In contrast, low levels of wall shear stress is believed to facilitate aneurysmal expansion.[15,16]

Because wall shear stress is derived from the velocity gradients along the vessel wall,[17] future studies regarding the role of wall shear stress depend on our ability to obtain reliable velocity information in and around intracranial aneurysms. While traditional vascular imaging has provided limited hemodynamic information, the recent advent of phase-contrast MRI (PC-MRI),[18] also referred to as four-dimensional flow (4D flow), offers a promising non-invasive imaging tool to provide a more thorough evaluation of flow patterns in intracranial aneurysms.

1.3 4D Flow and Its Limitations

4D flow is a time-resolved MR sequence that uses bipolar gradients to encode velocities in three (x-, y-, and z-) directions,[19] yielding a voxel-by-voxel velocity dataset that can be used to visualize flow patterns over time. After the application of the slice selective gradient, subsequent dephasing and rephasing gradients of equal magnitudes are subsequently applied in a single direction. Stationary spins will experience a net phase change of zero while moving spins (e.g. in flowing blood) will reflect a net phase shift since they will have experienced unequal magnitudes

of the bipolar gradients due to changes in their position. Since the resulting phase shift is proportional to the change in position, it can be directly attributed to a specific velocity, based on the assigned velocity encoding (VENC). To avoid aliasing, VENCs should be designated to include phase shifts slightly greater than ± 180°, although this should be adjusted for regions with lower flow.[18] This process is then repeated in the other two directions. A magnitude images is also acquired at each sampling time point, resulting in four data sets per each cardiac phase.

Despite 4D flow's ability to provide valuable velocity information, it has faced numerous limitations to being implemented in clinical settings. A complex and multi-step pre-processing (for unwrapping, segmentation, and background correction) is required before the phase datasets can be transformed, integrated and visualized with the magnitude image.[20] But a major limitation even before image processing occurs are the long scan times required to attain all four datasets. Scan times often last between 15-20 minutes,[21] increasing associated costs as well as the probability of motion artifacts.[22] Even after applying common acceleration methods such as parallel imaging,[23] 4D flow studies at our institution can last between 10-15 minutes, which is still too long to image aneurysms that may be at risk for rupture.

1.4 Compressed Sensing

Incorporation of compressed sensing (CS) into 4D flow sequences has been proposed as a way to reduce scan times. Compressed sensing is an MR undersampling technique based upon many concepts underlying data compression.[24] By using an incoherent, pseudo-random subsampling strategy (to avoid coherent aliasing[24]) and then applying advanced non-linear reconstruction methods to fill in the missing data points,[22,25] compressed sensing saves scan time by acquiring a *limited* dataset that is then used to reconstruct a full *k*-space. Compressed sensing is described in terms of acceleration factors, R, denoting the fraction of a *k*-space that is acquired.

As with other accelerated acquisition techniques, the addition of compressed sensing to 4D flow studies comes with tradeoffs. Applying compressed sensing to the velocity-encoding phase data sets means the original velocity samples are being blurred and spread out as the algorithm reconstructs the missing velocity data in the rest of *k*-space. Through this process, we can expect the original velocity data to also become blurred, likely resulting in underestimation of peak velocity and derived flow parameters like flow rates and wall shear stress. A recent study showed an experimental compressed sensing 4D flow sequence to have similar flow features and values as a standard accelerated acquisition in patient studies.[21] This study seeks to build upon these results, with the aim of better understanding the effects and possible limitations of varying compressed sensing acceleration factors at varied resolutions in *in vitro* 4D flow acquisitions.

1.5 Objective

The purpose of this study was to investigate whether aneurysmal flow patterns and parameters obtained with 4D flow acquisitions with varying levels of compressed sensing and at different resolutions are comparable with those obtained from the standard undersampled 4D flow acquisition routinely in use.

2. MATERIALS & METHODS

2.1 *In vitro* Three-Dimensional Phantom

This *in vitro* study employed a three-dimensionally printed negative gel phantom with a hollow lumen. It depicts a saccular aneurysm located between the anterior communicating and middle cerebral arteries, measuring approximately 1.3 cm at its widest region. The patient-specific phantom was selected due to the varied and complex flow patterns it can generate. In addition to

regions of low and high flow, the phantom was designed to also include a section representing the Circle of Willis, allowing for a region with recirculating flow.

2.2 Study Design for Experiments 1 and 2

Two experiments were conducted, each aimed at evaluating different aspects of 4D flow acquired with compressed sensing. Experiment 1 compared the effects of different compressed sensing acceleration factors (R=7.6, 12.8, and 16.6) to the standard undersampled 4D flow acquisition (Siemen's GRAPPA, a parallel-imaging acquisition with an acceleration factor R=2).

Experiment 2 used 4D flow with compressed sensing acceleration factor R=12.8 to test its effects among studies acquired at different isotropic resolutions: 0.5 mm, 1.0 mm, 1.5 mm, and 2.0 mm. The study with the highest resolution (0.5 mm) was used as the control. Figure 2.1 provides a graphical overview of the study design for both experiments.

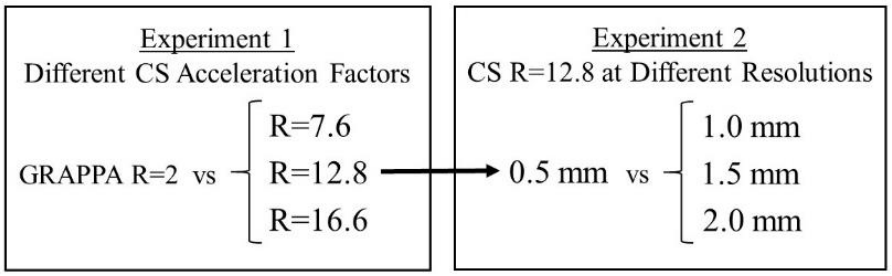

Figure 2.1 Study design of Experiment 1 and Experiment 2

2.3 4D Flow MR Acquisitions

All studies were acquired on a Siemens MAGNETOM Skyra 3T MRI scanner (Siemens Healthcare, Erlangen, Germany) at the Veteran's Affairs Medical Center (VAMC) in San Francisco, California. In both experiments, 5 L of water was infused with 5 mL of gadolinium and then circulated through the phantom using pulsatile flow. Flow rate was set to approximately 3 mL/sec. The imaging parameters of all imaging studies can be found in Table 1.

Table 2.1 Parameters of 4DF MR Acquisitions for Experiments 1 and 2

	Experiment 1				Experiment 2			
	GRAPPA	CS Acceleration Factors			Different Resolutions at CS R=12.8			
	R=2	R=7.6	R=12.8	R=16.6	0.5 mm	1.0 mm	1.5 mm	2.0 mm
VENC (cm/s)	120	120	120	120	120	120	120	120
FOV	240 x 180	240 x 180	240 x 180	240 x 180	240 x 180	240 x 180	240 x 180	240 x 180
Slice Thickness (mm)	1.0	1.0	1.0	1.0	0.5	1.0	1.5	2.0
Flip angle	15	15	15	15	15	15	15	15
TR (ms)	54.24	54.24	54.24	54.24	64.24	64.24	64.24	64.24
TE (ms)	3.71	3.53	3.53	3.53	4.76	4.47	4.76	4.76
NEX	1	1	1	1	1	1	1	1
Acceleration factor, R	2	7.6	12.8	16.6	12.8	12.8	12.8	12.8
No. of cardiac phases	16	16	16	16	14	14	14	14
Scan time (min:sec)	26:59	7:03	4:13	3:14	4:13	4:13	4:13	4:13

2.4 Flow Parameters Evaluated

The selected qualitative and quantitative flow parameters reflected some of the most commonly reported variables found in 4D flow.[26] Qualitative parameters included the velocity vectors and streamlines; quantitative parameters included individual voxel velocity components, peak velocity, flow rate, and wall shear stress.

2.5 Post-Processing

Since a major motivation of this study was to evaluate the feasibility of incorporating 4D flow into the clinical setting, studies were initially processed using a commercial, clinically-oriented software, CVI42 (CIRCLE Cardiovascular Imaging, Calgary, AB, Canada). CVI42's semi-automatic features were used to perform background correction, segmentation, flow processing, and analysis. All parameters except velocity components were obtained with CVI42.

To obtain the individual velocity components, as well as to validate the results provided by CVI42, studies were subsequently processed through an in-house engineering pipeline (In-House pipeline). To minimize intra-user variability, SimpleITK[27,28] was used to register all studies within a single experiment to each other. Segmentation of the phantom flow region was done with the Vascular Modeling Toolkit (VMTK)[29]; in-house Python scripts were then used for background

correction and flow processing. The processed 4D flow datasets were then visualized and analyzed using ParaView (Kitware, Clifton Park, NY, USA). All flow parameters except wall shear stress obtained using the In-House pipeline.

2.6 Visualization of Velocity Vectors and Streamlines

Velocity vectors and streamlines were generated in CVI42 and Paraview. CVI42 processing was conducted using their automatic visualization features for velocity vectors and streamlines; both were visualized at the maximum allowed level allowed of 20 particles/mL. Visualization of velocity vectors and streamlines in Paraview required significant more manual processing. A glyph filter was applied to the magnitude velocity dataset of each study. Velocity vectors were then created the StreamTracer filter. Streamlines were created using all velocity data points, with exception of the 0.5 mm study in Experiment 2 (every third point was used to prevent oversaturation). Final streamlines were composed of 30,000 points of size 2, with line widths of 1.75 (Experiment 1) and 1.25 (Experiment 2).

2.7 Velocity vector components

Figure 2.2 shows the strategy for evaluation of velocity vector components in both experiments. Studies from Experiment 1 were acquired with an isotropic resolution of 1.0 mm, allowing for a direct voxel-by-voxel comparison of velocity components using the In-House pipeline. The velocity data from the GRAPPA study was used as the standard for comparison.

Since studies in Experiment 2 were acquired at different isotropic resolutions, a direct comparison of velocity components could not be implemented using the same approach. Instead, over 100,000 sample points were obtained in the exact same locations throughout the registered phantom volumes. The 0.5 mm resolution study did not include a portion of the phantom inlet;

thus, sample points from inlet regions in the other studies were not included in the analysis. The velocity components for each subsampled point were then interpolated, weighing the velocity information from its neighboring voxels. The velocity components of the 1.0 mm, 1.5 mm, and 2.0 mm studies were compared to those of the 0.5 mm study.

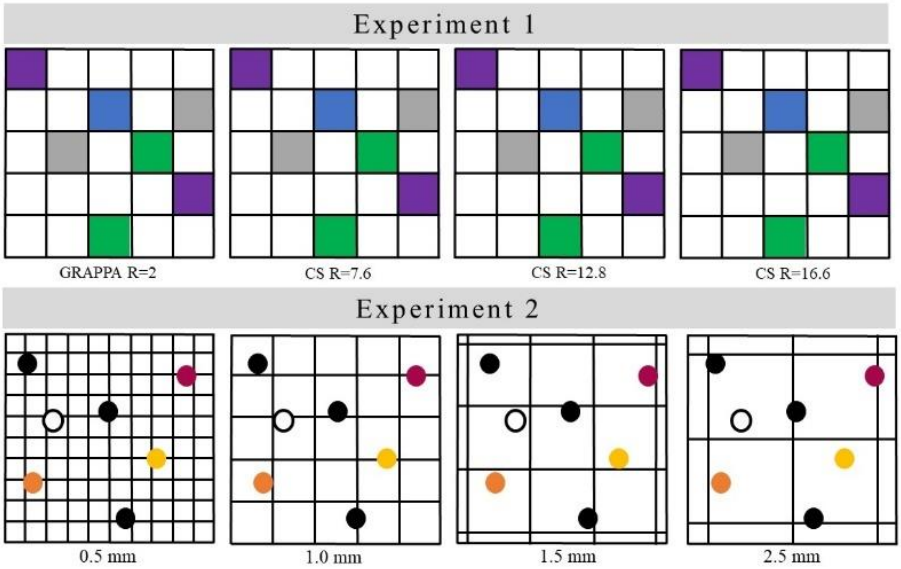

Figure 2.2 Strategy for comparison of velocity components. Velocity components in Experiment 1 were conducted on a voxel-by-voxel basis, represented by the same color across different studies. Experiment 2 required sampling points from each dataset and interpolating its velocity components from its neighboring voxels before comparing them.

2.8 Peak velocity, flow rate and WSS

Peak velocity, flow rate, and WSS values were evaluated at three distinct slices around the aneurysms: the inlet; main body of the aneurysm (coronal view); and the outlet (Figure 2.3). In CVI42, three planes were manually positioned at the three locations on the individual studies, using planes in the first (GRAPPA) study as visual references. Within each plane, the specific regions of interest were manually edited to ensure the contour aligned with the vessel wall. These planes were then replicated in Paraview using various filters. Since all studies within a single

experiment were registered to each other, the exact slice coordinates were uniformly applied. The peak velocity, flow rate, and WSS of each plane and slice were then obtained for a cardiac cycle.

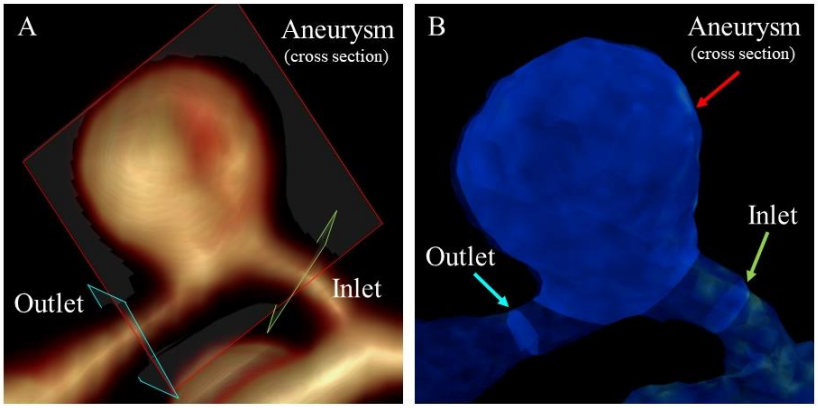

Figure 2.3 Planes of interest in (A) CVI42 and (B) In-House pipeline for the evaluation of peak velocity, flow rate, and wall shear stress

2.9 Data Analysis

Data used for the visualization of velocity vectors and streamlines, and the component analysis were evaluated at systole to ensure the widest range of values. Velocity vectors and streamlines generated in CVI42 and the In-House pipeline; they were qualitatively described and compared against the experiment's respective control study.

Analysis of velocity components were done using In-House Python scripts. Velocity components were plotted against their experiment's control data; linear regression lines and correlation coefficients were then calculated. To gain a thorough understanding of the effects of compressed sensing on voxels based on their position within a vessel, this was done for all voxels in the data set; voxels closest to the wall, where partial voluming is likely starting to take effect; and voxels furthest from the wall. Bland-Altman plots were also generated to evaluate the limits of agreements for the magnitude velocities in both experiments.

The peak velocities data from CVI42 were plotted on a single graph; the data for the same parameter obtained through the In-House pipeline was similarly plotted on a separate graph. This was repeated for the flow rates and wall shear stress parameters. Plotting two separate graphs allowed evaluation of the effects of the test variables within and amongst each processing pipeline. The goal was to validate any observed trends by the other pipeline.

3. RESULTS

3.1 Visualization of Velocity Vectors and Streamlines

The velocity vectors and streamlines generated by CVI42 and In-House pipeline show stark differences in their visualization capabilities. CVI42 provides very sparse velocity vectors and streamlines for all 4D flow studies in both experiments (Figures 3.1 and 3.2). The In-House pipeline yielded adequate velocity vectors, streamlines, and overall flow patterns.

In Experiments 1 and 2, velocity vectors and streamlines generated by CVI42 are mostly isolated to the inlet and bifurcation, mainly in the opposite direction of the aneurysm with only a few vectors appearing in the aneurysm itself. Overall, CVI42 is unable to reflect flow patterns through the aneurysm or distal regions, likely due to the fact that CVI42 visualizations were limited to 20 particles per mL. Although this may be sufficient for flow visualization in larger vessels with larger flow volumes, it is clearly insufficient for visualizing flow in intracranial vessels.

In contrast, velocity vectors and streamlines processed and visualized through the In-House pipeline depict flow throughout the entire phantom. In each study, a range of velocities can be seen at the phantom inlet, with high velocities vectors detected at the bifurcation before splitting into two branches. A vortex pattern inside the aneurysm can be seen in each study. All distal regions reflect low velocity flow, with vectors showing high directional variability.

3.1.1 Experiment 1: Visualization of Velocity Vectors and Streamlines

Figure 3.1 shows velocity vectors and streamlines for Experiment 1. Experiment 1's velocity vectors show little variability with increasing acceleration factors. Most observable differences occur in vectors located along the aneurysm wall and outlet. Streamlines show greater variability with different acceleration factors. Interestingly, all studies compressed sensing acceleration factors show streamlines going through the bifurcation into at least one branch and often the aneurysmal branch, which is not visible on the GRAPPA study. All streamlines depict a vortex in the aneurysm, although it is more blurred in the streamlines from CS R=16.8. The stenosis at the distal end of the aneurysm is preserved in all studies.

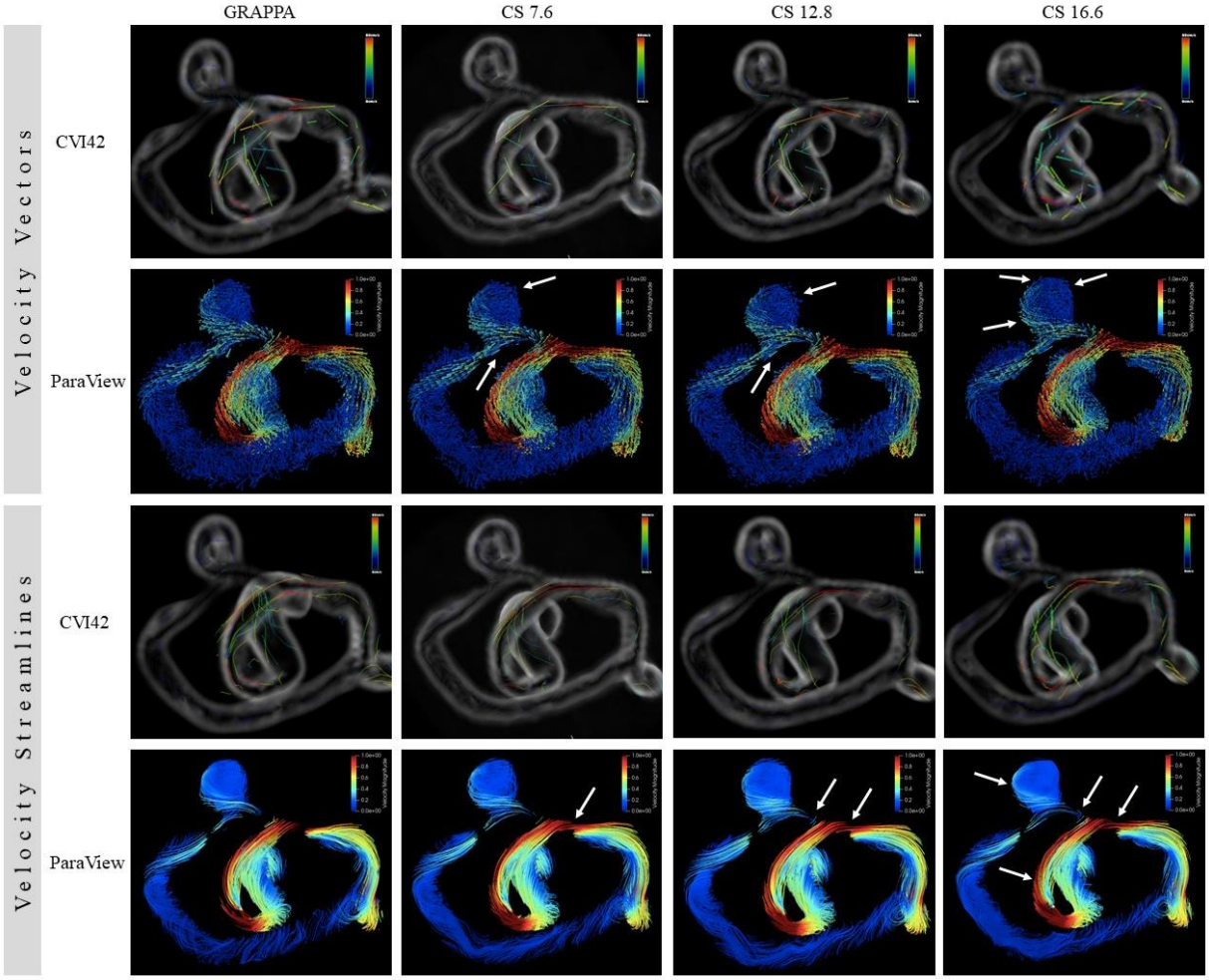

Figure 3.1 Velocity vectors and streamlines at systole for Experiment 1. Arrows indicate locations where deviations from GRAPPA study are observed.

The velocities in the CS R=7.6 streamlines most closely resemble those of the GRAPPA study, while the CS R=16.6 streamlines appear to underestimate the velocities throughout the entire phantom, despite having more streamlines. An important but subtle difference occurs in streamlines along the inlet and bifurcation, which appear darker in the CS R=16.6 than in the GRAPPA or other compressed sensing studies. This presents a clear limitation of using high compressed sensing acceleration factors; overestimation in individual velocities would further be compounded in the calculation of flow parameters like flow rate and wall shear stress.

3.1.2 Experiment 2: Visualization of Velocity Vectors and Streamlines

In Experiment 2, the effects of different resolutions at CS R=12.8 become apparent upon evaluation of the velocity vectors and streamlines (Figure 3.2). There is a noticeable decrease in the number of vectors as the voxel size increases, with 2.0 mm having the lowest density of vectors.

Apart from a decreasing number of velocity vectors, reflecting the reduction in the number of voxels, we can observe a decrease in the velocity magnitudes, specifically along the inlet, branch opposite the aneurysm, and the aneurysm outlet. In these three regions we see a decrease in the highest velocities, reflecting underestimation of velocities as the resolution decreases.

Although the 0.5 mm resolution study provides the greatest number of velocity vectors throughout the phantom, its streamlines are sparser than in the 1.0 mm, 1.5 mm, and 2.0 mm studies. As resolution increases, we observe a decrease in the velocities around the inlet turn, at the bifurcation, and the branch opposite the aneurysm. We also see a decrease in the velocities at the inlet of the aneurysm.

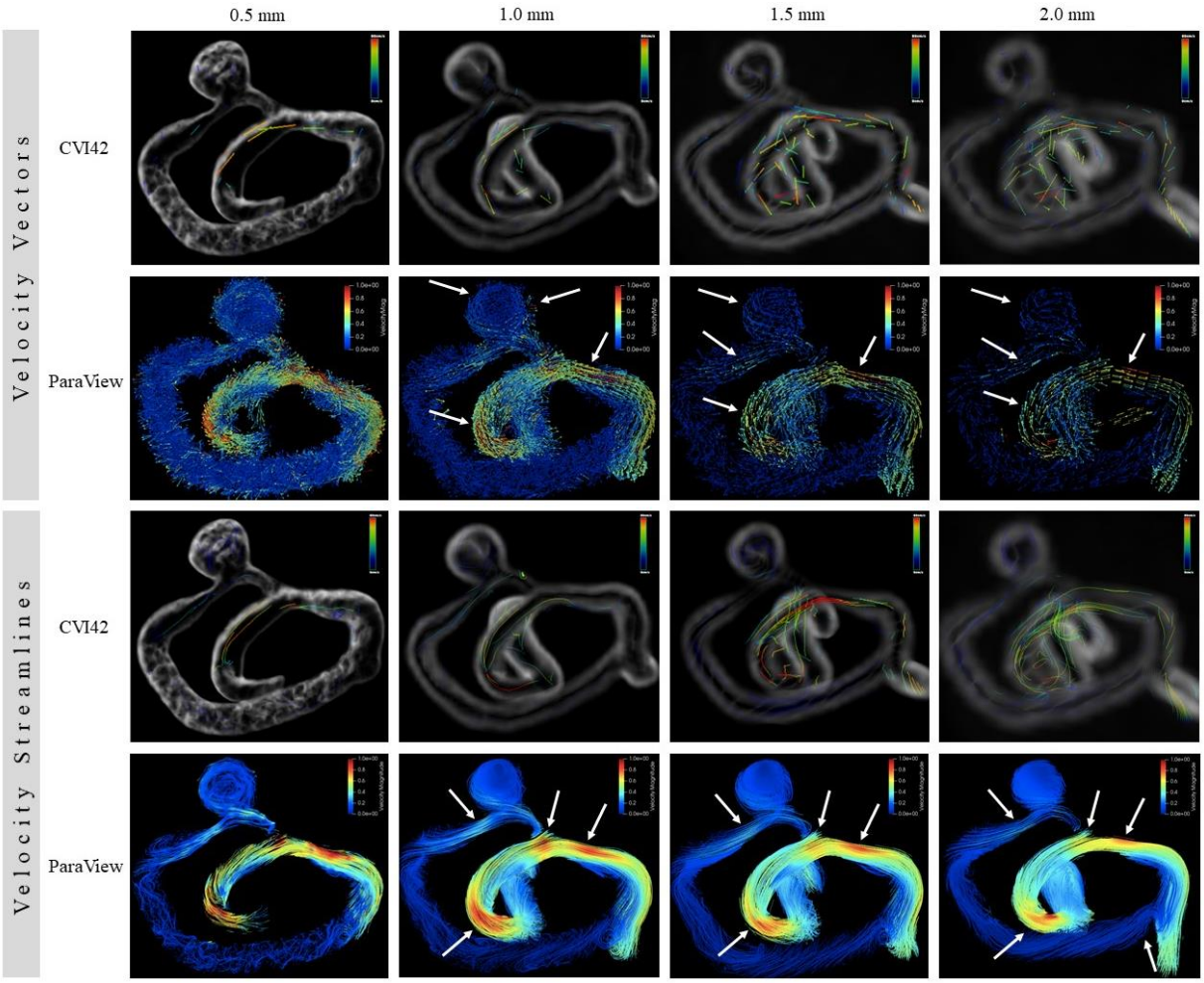

Figure 3.2 Velocity vectors and streamlines at systole for Experiment 2. Arrows indicate locations where deviations from 0.5 mm resolution study are observed.

3.2 Comparison of Velocity Components

3.2.1 Experiment 1: Velocity Components at Different Compressed Sensing Acceleration Factors

The plots comparing the magnitude velocity components at systole of the compressed sensing acquisitions with those of the standard GRAPPA 4D flow acquisition are shown in Figure 3.3. As expected, both the regression lines for the magnitude velocities decrease as acceleration factors increase, indicating an inverse relationship between them.

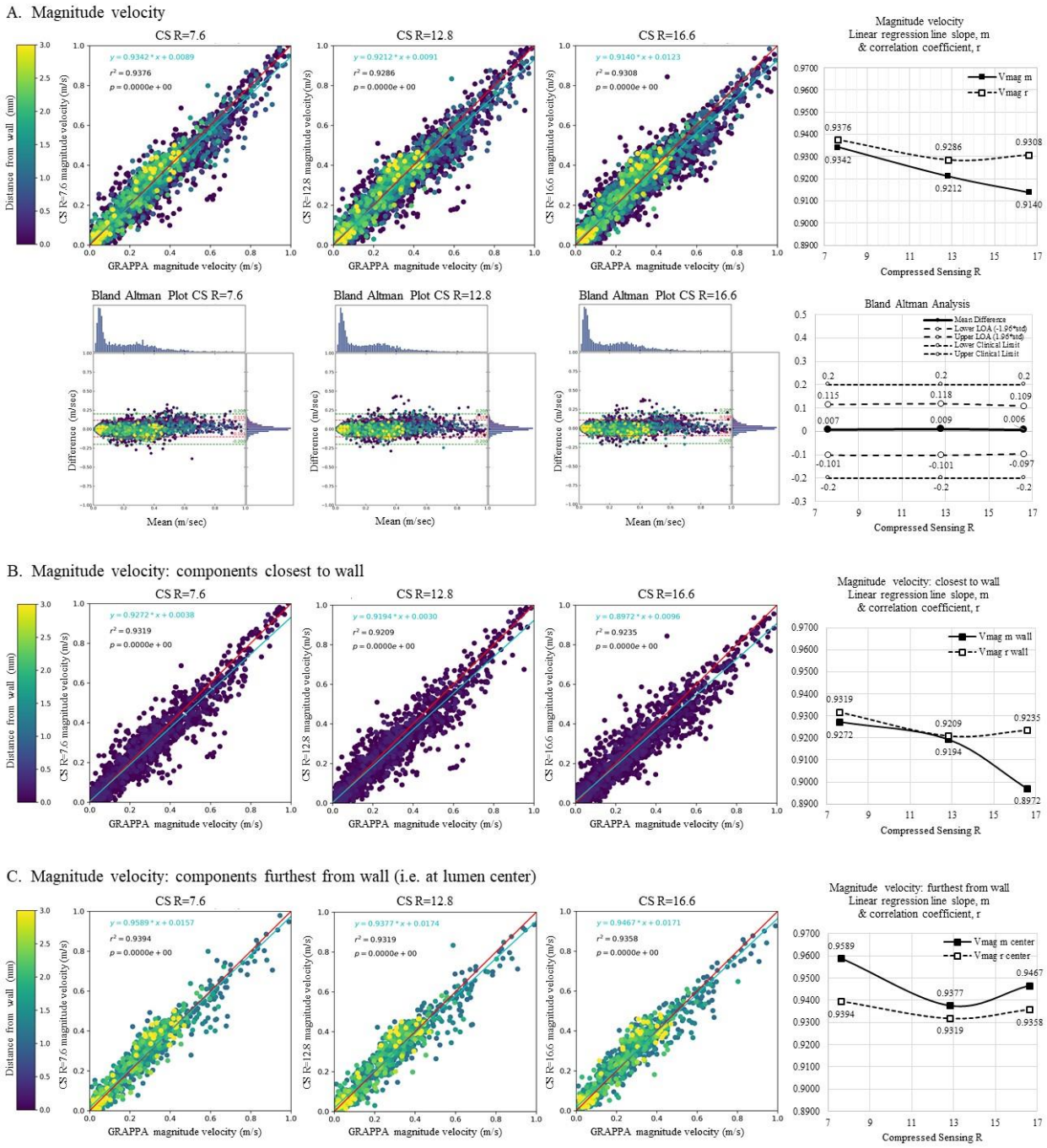

Figure 3.3 Comparison of magnitude velocity components in Experiment 1. A. The individual magnitude velocity components of each experimental acceleration factor (from left to right: CS R=7.6, 12.8, and 16.6) is plotted against its corresponding velocity components in the GRAPPA study. The graphs on the right show the regression slopes and correlation coefficients of each study. Bland Altman plots detail limits of agreement at different acceleration factors. B. Velocity component analysis for velocity components closest to the wall. C. Velocity component analysis for the velocity components furthest from the wall (i.e. closest to the center).

In general, although the magnitude velocities from the compressed sensing acquisitions are likely underestimating the corresponding velocities obtained in the GRAPPA study, they reflect a strong linear relationship, with all regression lines having $m > 0.9140$ and $r > 0.9286$. The relationship falls slightly for velocity components located closest to the wall, with $m > 0.8972$ and $r > 0.9209$, reflecting partial voluming effects in those voxels. In contrast, velocity components located furthest from the wall reflect the highest linear relationship ($m > 0.9377$) and strongest correlations ($r > 0.9319$), even at the highest CS R=16.6. Slight deviations in the regression and correlations are observed for velocity components obtained with CS R=16.6, further suggesting this may be the limit of compressed sensing acceleration factors.

The Bland Altman analysis for magnitude velocities further supports this. The average difference between GRAPPA and compressed sensing velocities components ranges from 0.006 and 0.009, indicating compressed sensing only slightly underestimates the magnitude velocities. The limits of agreements (containing approximately 95% of the data) decrease as acceleration factors increase, starting from ± 0.108 (for CS R=7.6) and progressing to ± 0.109 (CS R=12.8), and ± 0.103 (for CS R=16.6). Yet all fall within the clinical limit of agreement of ± 0.2, indicating overall good agreements amongst the different compressed sensing acceleration factors.

3.2.2. Experiment 2: Velocity Components of Different Resolutions with Compressed Sensing R=12.8

Experiment 2 shows high variability amongst the systolic velocity components acquired at different resolutions with a compressed sensing acceleration factor of R=12.8, as shown in Figure 3.4. Although the linear regression slope for the magnitude velocity components of the 1.0 mm acquisition is quite high (0.9970), its correlation coefficient is much lower (0.8776), reflecting a

greater degree of variation (in both directions) in the compressed sensing velocity components compared to those from GRAPPA.

Regression slopes and correlation coefficients continue to decrease at lower resolutions, with the 2.0 mm acquisition having the lowest regression slope (m=0.8346) and correlation coefficient (r=0.8106). For velocity components from voxels located closest to the wall, partial voluming effect can be observed as the regression slope and correlation coefficient start at m=0.8601 and r=0.6146 for 1.0 mm and continue to decrease at 1.5 mm and 2.0 mm. In contrast, the velocity components from voxels furthest from the wall start with regression lines above 0.9 at resolutions of 1.0 mm and 1.5 mm, before increasing to m=1.0318 and then dropping to m=0.8240. Although the correlation coefficients range from 0.8240 (2.0 mm) and 0.9407 (1.5 mm), they are still higher than the corresponding values for components along the wall, even at 2.0 mm, indicating there is little partial volume effect occurring in this region. Overall, the velocity components coming from the center of the lumen in 1.0 mm and 1.5 mm resolution studies most reliably approximate the velocity components from the GRAPPA velocity dataset.

The Bland Altman analysis for magnitude velocities further supports this. The average difference between the GRAPPA and compressed sensing velocities components ranges from 0.014 and 0.030, indicating increasing underestimations of the magnitude velocities as the voxel size increases. The limits of agreements increase along with voxel size, from ± 0.140 (for 1.0 mm) to ± 0.150 (1.5 mm) to ± 0.165 (2.0 mm). The limits of agreement for 1.0 mm and 1.5 mm resolutions fall comfortably below the clinical limits of agreement; the limit of agreement for 2.0 mm is very close to that of the upper clinical limit, indicating a possible limitation of voxel size when studies are acquired with a CS R=12.8.

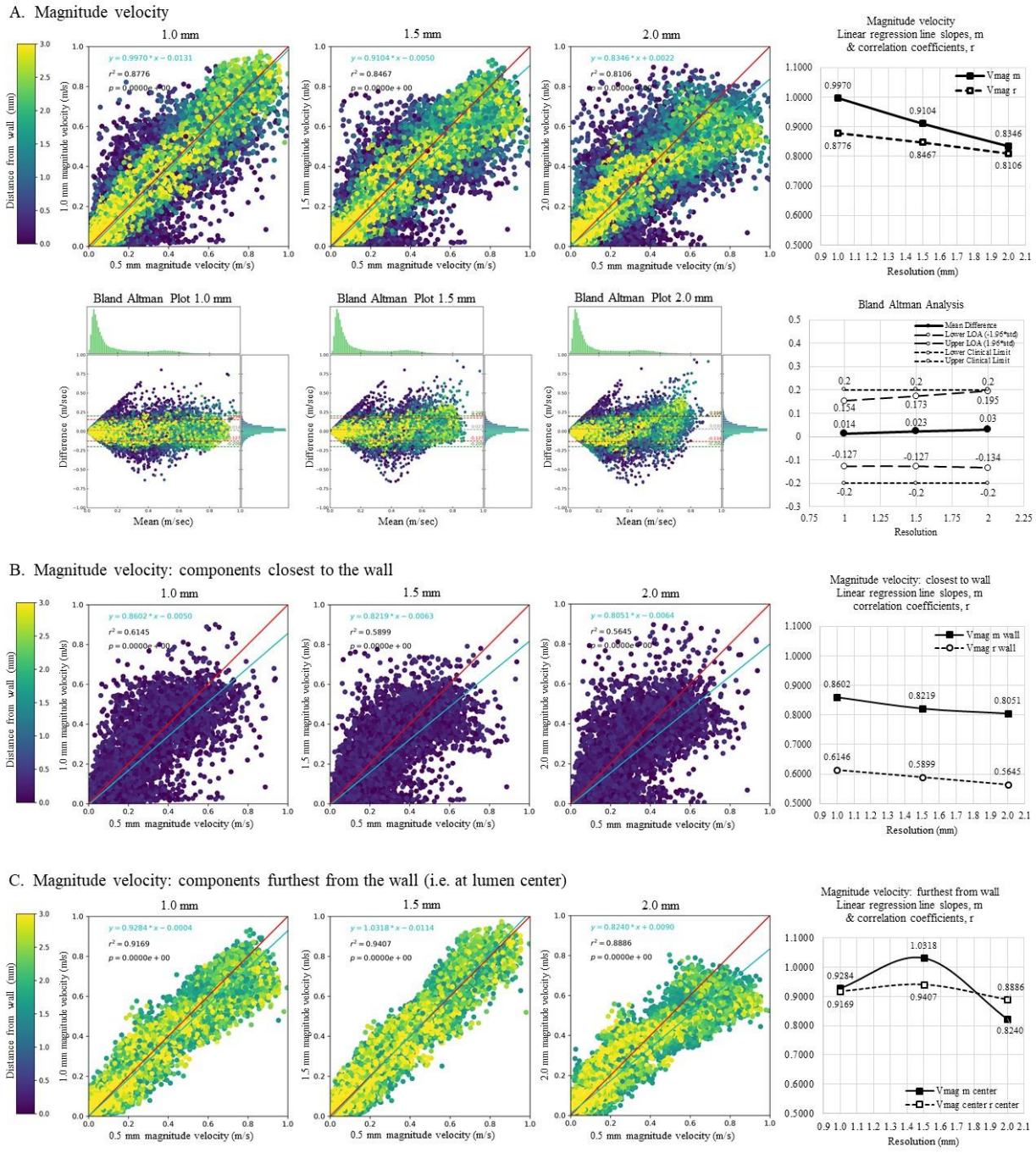

Figure 3.4 Comparison of magnitude velocity components in Experiment 2. A. The individual magnitude velocity components of each resolution (from left to right: 1.0 mm, 1.5 mm, and 2.0 mm), acquired with CS R=12.8, is plotted against the velocity components of the GRAPPA study. The graph on the right show the regression slopes and correlation coefficients of each study, relative to each other. Bland Altman plots detail limits of agreement for each resolution. B. Velocity component analysis for velocity components closest to the wall. C. Velocity component analysis for the velocity components furthest from the wall (i.e. closest to the center).

3.3 Peak Velocities, Flow Rates & Wall Shear Stress

Obtaining reliable values for peak velocity, flow rate, and wall shear stress proves to be challenging regardless of the processing pipeline employed. In general, there is great variability in the peak velocity, flow rate, and wall shear stress data obtained for each plane of interest. Data presented for Experiment 1 and Experiment 2 is limited to the inlet plane, since similar variability was also observed in the aneurysm cross-sectional and outlet planes.

3.3.1 Experiment 1: Peak Velocities, Flow Rates, and Wall Shear Stress at Different Acceleration Factors

CVI42 shows studies with compressed sensing overestimate peak velocity throughout most of the cardiac cycle when compared to the GRAPPA study, although there is great variability amongst themselves (Figure 3.5). The In-House pipeline reflects the opposite trend; all compressed sensing studies severely underestimate the peak velocities, with a noticeable difference in scales between the GRAPPA and all of the compressed sensing studies.

Although the flow rate curve shapes of the GRAPPA and compressed sensing acquisitions resemble each other, there is variability amongst them throughout the entire cardiac cycle. Flow rate curves generated through Paraview reflect less variability, although they appear to be significantly lower than the values obtained from CVI42.

Wall shear stress curves in the studies obtained with compressed sensing are lower than that of the GRAPPA study, although their order (CS R=12.8 > 16.6 > 7.6) is unexpected. These results are not able to be validated since the In-House pipeline does not yet have a reliable way to compute wall shear stress.

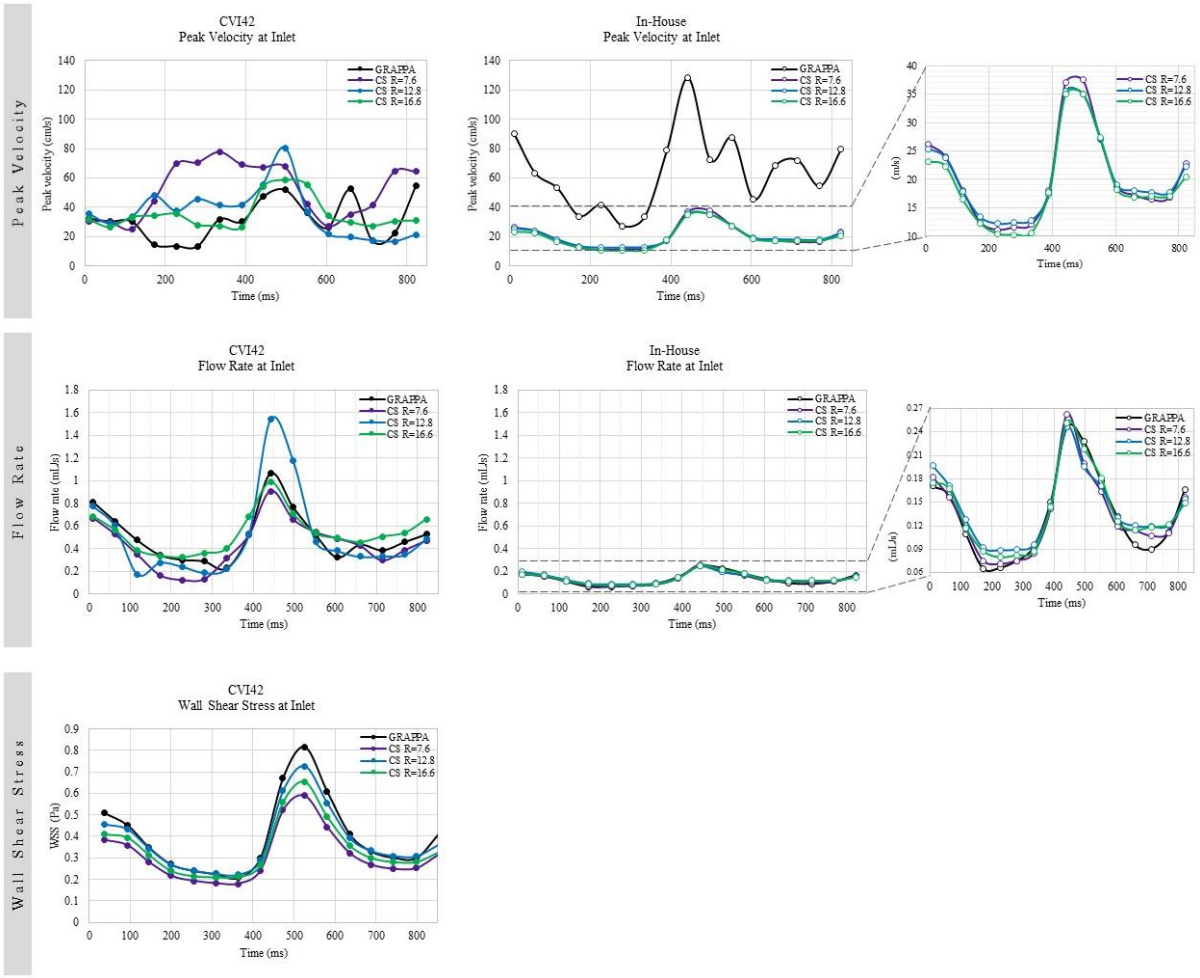

Figure 3.5. Peak velocities, flow rates, and wall shear stress for Experiment 1

3.3.2 Experiment 2: Peak Velocities, Flow Rates, and Wall Shear Stress of Different Resolutions with Compressed Sensing R=12.8

CVI42 and In-House pipeline both show the lower resolution scans in Experiment 2 underestimating the peak velocities throughout the cardiac cycle (Figure 3.6). There is more variety in the peak velocity curves generated in CVI42, specifically of the 0.5 mm, which also appears much higher than its counterpart generated through the In-House pipeline. It is difficult to ascertain a trend amongst the curves for each resolution as well as within each individual pipeline.

Flow rate curves generated in CVI42 show similar shapes, with the exception of the 2.0 mm curve, although their values show little overlap. Additionally, the flow rate curves from the

1.5 mm and 2.0 mm studies show retrograde flow, particularly after systole, which is not observed in the In-House pipeline. The curves from the In-House pipeline show less shape variability, but their values are significantly lower than those from CVI42. The trends observed in CVI42 data, with the majority of the curves underestimating the 0.5 mm flow rates, are not observed in the In-House data, with 1.0, 1.5, and 2.0 mm curves all reflecting higher flow rates than the 0.5 mm scan.

The wall shear stress curves generated by CVI42 show very similar shapes for the different voxel resolutions throughout the cardiac cycle. The data suggests wall shear stress at a specific location decreases as the voxel sizes increases; although this is the expected result, it cannot be verified since an In-House wall shear stress pipeline has not yet been established.

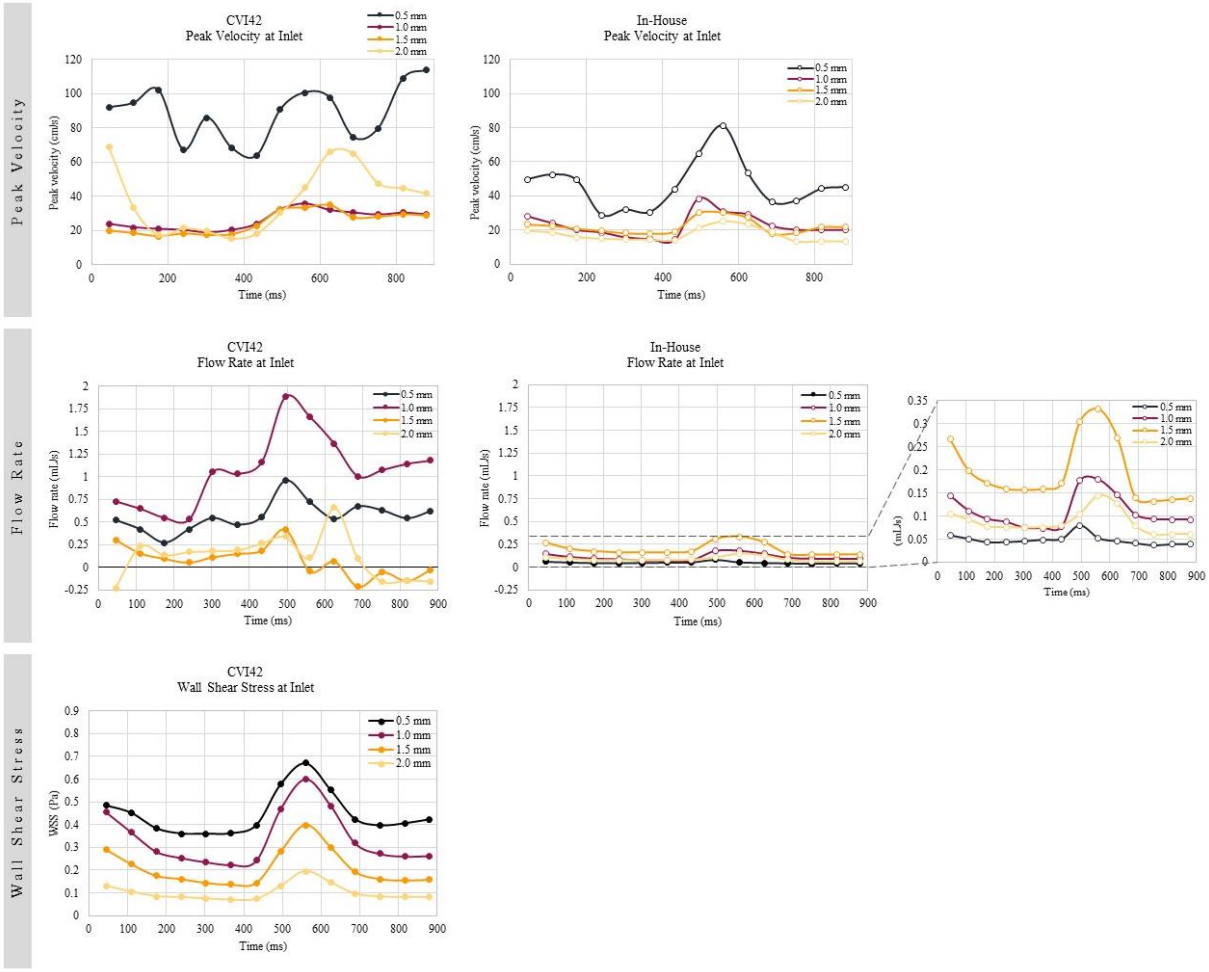

Figure 3.6. Peak velocities, flow rates, and wall shear stress for Experiment 2

4. DISCUSSION, FUTURE WORKS AND CONCLUSION

The addition of compressed sensing to 4D flow MRI shows scan times can be reduced to approximately 4-7 minutes, moving such studies closer to being applied in the clinical setting.

Analysis of velocity vectors in Experiment 1 show slight changes along the aneurysm wall and outlet, but retain the overall flow patterns even with increased compressed sensing acceleration factors. Streamlines similarly reflect the same flow patterns, although CS R=16.6 appears to overestimate the velocities along the inlet and bifurcation; this likely indicates the limit to compressed sensing acceleration factors lies between R=12.8 and R=16.6. As in Experiment 1, velocity vectors in Experiment 2 reflect the overall flow pattern in the phantom. Although the 2.0 mm study has fewer velocity vectors, an advantage of working with a robust visualization application like Paraview is the ability to adjust and amplify the number of vectors if necessary. Although the streamlines at 1.0 mm offer a close estimation to the streamlines in the 0.5 mm study, velocities in the 1.5 mm and 2.0 mm studies progressively underestimate the 0.5 mm velocities, specifically at the inlet and bifurcation. This occurs because as voxel size increases, higher velocities become averaged out by the addition of other, lower velocity components.

Evaluation of the qualitative parameters also highlight differences between the two 4D flow post-processing pipelines employed in this study. Although the clinical software evaluated, CVI42, is very user friendly and consolidates many post-processing steps, it provides overall sparse flow visualization. It also reflects great variability in the quantitative parameters evaluated, as discussed below. The results from the In-House engineering pipeline yields less variability although the data often differs in scale when compared to CVI42. Clearly, *how* 4D flow is processed matters and can significantly impact what conclusions can be drawn from the data.

Analyses of the velocity components indicate a high degree of fidelity in the velocity data from 4D flow studies acquired with the low (R=7.6) and moderate (R=12.8) compressed sensing acceleration factors (Experiment 1), with regression slopes and correlation coefficients generally above 0.9. Experiment 2 shows a moderate level of compressed sensing has a greater blurring effect on the velocity data, particularly in voxels located along the wall, as resolution decreases. Magnitude velocity components in higher resolutions (0.5 mm and 1.0 mm) maintain linear regression slopes above 0.90, although their correlations are less 0.9. This is likely to improve with lower levels of compressed sensing (i.e. at R=7.6), as shown in Experiment 1. A closer evaluation based on a velocity component's position relative to the wall indicates greater fidelity than components located furthest from the wall (i.e. closer to the center of the lumen). Overall, analysis of the individual velocity components and their limits of agreement confidently imply velocity data obtained with low to moderate compressed sensing acceleration factors (R=7.6 or 12.8) acquired at lower (0.5-1.0 mm) resolutions are comparable to the standard GRAPPA study.

This study has numerous limitations that should be kept in mind when evaluating its results. A major limitation is that a true "gold standard" was not used to evaluate the 4D flow with compressed sensing acquisitions against. As previously mentioned, the standard 4D flow acquisition employed a GRAPPA sequence, which is itself an undersampling technique. This was done due to the fact that GRAPPA is already widely used with 4D flow imaging, as well as the long scan time that would be required to image a fully-sampled 4D flow acquisition. A possible solution would be to generate a three-dimensional computational model and mesh of the aneurysm phantom and conduct a computational fluid dynamic simulation, which is currently in the works.

There are also many limitations relating to the clinical processing software, which had difficultly post-processing most compressed sensing studies. Flow was often detected outside the

lumen of the gel phantom while underestimating the amount of flow inside the lumen; CVI42 allows for manual removal of static and air detected regions inside the phantom lumen but unfortunately does not allow removal of flow-detected regions throughout the rest of the phantom. Setting a high mask threshold to maximize flow inside the lumen most likely affected the accuracy of the background correction and subsequently required significant manual segmentation to limit the flow to the appropriate regions of the phantom. This, along with the smoothing effects of the compressed sensing non-linear reconstruction on the magnitude image, likely contributed to intra-user variability amongst all studies, for both Experiments 1 and 2.

The inability to position the analysis planes using a coordinate system also likely contributed to the high variability in the CVI42 data, since we cannot be certain they were placed in the exact same location. Additionally, the contoured region of interest on the planes changed area throughout the cardiac cycle, which likely explains the wide range in its calculated flow rates. This feature is probably advantageous when processing *in vivo* studies, with expanding and contracting vessels, yet not applicable in the solid, non-deformable phantom flow model used here.

Difficulties in generating the velocity vectors and streamlines in CVI42 further draw attention to the fact that most of CVI42's post-processing tools are FDA-cleared for cardiac applications but are still experimental for neuro-vasculature applications. While 20 particles/mL is probably sufficient for visualizing vector fields and streamlines in the aorta or pulmonary arteries, which are larger than the majority of intracranial vessels, it is evidently insufficient for visualizing the anterior communicating and middle cerebral arteries.

Due to its proprietary nature, we are unable to know exactly how CVI42 is calculating many of the quantitative parameters. For example, we believe it calculates flow rate by multiplying the average velocity within a contour by its (changing) area, since the flow rate curves appear all

to have a similar shape, but cannot be certain about this. The wide variability in the peak velocities also reduces confidence in CVI42's ability to accurately evaluate a small, specific subset of the velocity data. Average velocity could be a more robust parameter to use in lieu of peak velocity, which depends on a single velocity value of an analysis plane, thus more susceptible to outliers.

CVI42 provides the maximum and average wall shear stress along the vessel circumference, but does not provide the value of the lowest wall shear stress nor their exact locations of these values, which would be of great interest when evaluating aneurysmal growth. And although there are clear trends in the wall shear stress data provided by CVI42, the results are cannot be validated through the In-House pipeline.

The In-House processing pipeline also presents with its own limitations, apart from lacking an established method to obtain wall shear stress values. This pipeline requires significantly more time and technical expertise to process studies in multiple steps, in multiple software environments, also necessitating additional points of data transfer. Although this pipeline facilitates for easier trouble shooting, such a post-processing workflow would not be feasible to implement in a clinical setting.

Another limitation of the In-House pipeline includes segmentation of the flow region. Since the phantom was a solid model with a flow lumen that does not change dimensions, segmentation could be done using the magnitude image and then applied throughout the entire cardiac cycle. But this would not be feasible when processing *in vivo* studies, where vessels dilate and contract throughout the cardiac cycle. Segmentation at each phase of a study would require significantly more time and multiply the number of datasets to be processed for a single study.

Lastly, although the phantom was created from patient-specific data, *in vivo* anatomy is undoubtedly more complex. Signal from surrounding tissue may affect the compressed sensing

reconstruction differently and the presence of additional vessels may affect the hemodynamics observed. The results of *in vivo* studies, currently underway, will help evaluate the true effects of 4D flow with compressed sensing in patients with intracranial aneurysms and provide the opportunity to evaluate the effects of compressed sensing in aneurysms with varying shapes and sizes.

4.1 Conclusion

The analysis of the velocity components showed velocity data can be reliably obtained using 4D flow with compressed sensing, particularly when acquired with lower acceleration factors at higher resolutions; visual analysis of the velocity vectors and streamlines further supports this. Yet high variability in the other flow parameters highlights another known limitation of 4D flow imaging: namely the need to establish a reliable, robust yet efficient, and validated workflow.

5. REFERENCES

1. NINDS. Cerebral Aneurysm Fact Sheet. *Cerebral Aneurysm Fact Sheet* (2018).
2. Toth, G. & Cerejo, R. Intracranial aneurysms: Review of current science and management. *Vasc. Med. (United Kingdom)* **23**, 276–288 (2018).
3. Brown, R. D. & Broderick, J. P. Unruptured intracranial aneurysms: Epidemiology, natural history, management options, and familial screening. *Lancet Neurol.* **13**, 393–404 (2014).
4. Vega, C., Kwoon, J. V. & Lavine, S. D. Intracranial aneurysms: Current evidence and clinical practice. *Am. Fam. Physician* **66**, 601–608 (2002).
5. Thompson, B. G. *et al. Guidelines for the Management of Patients With Unruptured Intracranial Aneurysms: A Guideline for Healthcare Professionals From the American Heart Association/American Stroke Association*. *Stroke; a journal of cerebral circulation* **46**, (2015).
6. Etminan, N. & Rinkel, G. J. Unruptured intracranial aneurysms: Development, rupture and preventive management. *Nat. Rev. Neurol.* **12**, 699–713 (2016).
7. Ajiboye, N., Chalouhi, N., Starke, R. M., Zanaty, M. & Bell, R. Unruptured Cerebral Aneurysms: Evaluation and Management. *Sci. World J.* **2015**, (2015).
8. Backes, D. *et al.* PHASES Score for Prediction of Intracranial Aneurysm Growth. *Stroke* **46**, 1221–1226 (2015).
9. Zhang, X. *et al.* Total Hospital Costs and Length of Stay of Endovascular Coiling Versus Neurosurgical Clipping for Unruptured Intracranial Aneurysms: Systematic Review and Meta-Analysis. *World Neurosurg.* **115**, 393–399 (2018).
10. Bijlenga, P. *et al.* PHASES Score for the Management of Intracranial Aneurysm: A Cross-

Sectional Population-Based Retrospective Study. *Stroke* **48**, 2105–2112 (2017).

11. Kim, B. J. *et al.* Small versus Large Ruptured Intracranial Aneurysm: Concerns with the Site of Aneurysm. *Cerebrovasc. Dis.* (2017). doi:10.1159/000452347
12. Longo, M. *et al.* Role of Hemodynamic Forces in Unruptured Intracranial Aneurysms: An Overview of a Complex Scenario. *World Neurosurg.* **105**, 632–642 (2017).
13. Munarriz, P. M. *et al.* Basic Principles of Hemodynamics and Cerebral Aneurysms. *World Neurosurg.* **88**, 311–319 (2016).
14. Sforza, D. M., Putman, C. M. & Cebral, J. R. Hemodynamics of Cerebral Aneurysms. *Annu. Rev. Fluid Mech.* **41**, 91–107 (2009).
15. Savastano, L. E., Bhambri, A., Andrew Wilkinson, D. & Pandey, A. S. *Biology of Cerebral Aneurysm Formation, Growth, and Rupture*. *Intracranial Aneurysms* (Elsevier Inc., 2018). doi:10.1016/b978-0-12-811740-8.00002-2
16. Boussel, L. *et al.* Aneurysm growth occurs at region of low wall shear stress: Patient-specific correlation of hemodynamics and growth in a longitudinal study. *Stroke* **39**, 2997–3002 (2008).
17. Zimmermann, J. *et al.* Wall shear stress estimation in the aorta: Impact of wall motion, spatiotemporal resolution, and phase noise. *J. Magn. Reson. Imaging* **48**, 718–728 (2018).
18. Markl, M. *et al.* Time-resolved three-dimensional phase-contrast MRI. *J. Magn. Reson. Imaging* **17**, 499–506 (2003).
19. Markl, M., Frydrychowicz, A., Kozerke, S., Hope, M. & Wieben, O. 4D flow MRI. *J. Magn. Reson. Imaging* **36**, 1015–36 (2012).
20. Schnell, S., Wu, C. & Ansari, S. A. Four-dimensional MRI flow examinations in cerebral and extracerebral vessels - Ready for clinical routine? *Curr. Opin. Neurol.* **29**, 419–428

(2016).

21. Liu, J. *et al.* Highly accelerated intracranial 4D flow MRI: evaluation of healthy volunteers and patients with intracranial aneurysms. *Magn. Reson. Mater. Physics, Biol. Med.* (2018). doi:10.1007/s10334-017-0646-8

22. Jaspan, O. N., Fleysher, R. & Lipton, M. L. Compressed sensing MRI: A review of the clinical literature. *Br. J. Radiol.* **88**, 1–12 (2015).

23. Turski, P. *et al.* Neurovascular 4DFlow MRI (Phase Contrast MRA): emerging clinical applications. *Neurovascular Imaging* **2**, 0–11 (2016).

24. Lustig, M., Donoho, D. & Pauly, J. M. Sparse MRI: The application of compressed sensing for rapid MR imaging. *Magn. Reson. Med.* **58**, 1182–1195 (2007).

25. Geethanath, S. *et al.* Compressed sensing MRI: A review. *Crit. Rev. Biomed. Eng.* **41**, 183–204 (2013).

26. Puiseux, T. *et al.* Reconciling PC-MRI and CFD: An in-vitro study. *NMR Biomed.* **32**, 1–14 (2019).

27. Lowekamp, B. C., Chen, D. T., Ibáñez, L. & Blezek, D. The design of simpleITK. *Front. Neuroinform.* **7**, 1–14 (2013).

28. Yaniv, Z., Lowekamp, B. C., Johnson, H. J. & Beare, R. SimpleITK Image-Analysis Notebooks: a Collaborative Environment for Education and Reproducible Research. *J. Digit. Imaging* **31**, 290–303 (2018).

29. Antiga, L. *et al.* An image-based modeling framework for patient-specific computational hemodynamics. *Med. Biol. Eng. Comput.* **46**, 1097–1112 (2008).

Publishing Agreement

It is the policy of the University to encourage the distribution of all theses, dissertations, and manuscripts. Copies of all UCSF theses, dissertations, and manuscripts will be routed to the library via the Graduate Division. The library will make all theses, dissertations, and manuscripts accessible to the public and will preserve these to the best of their abilities, in perpetuity.

I hereby grant permission to the Graduate Division of the University of California, San Francisco to release copies of my thesis, dissertation, or manuscript to the Campus Library to provide access and preservation, in whole or in part, in perpetuity.

Author Signature Virginia Hinojosa Date 09/09/2019